



RESEARCH ARTICLE

10.1002/2015EA000102

Key Points:

- Radar cross sections of rimed snowflakes were computed from 3-D models
- Significant differences exist between 3-D models and spheroids
- Three-frequency radar can be used to detect snowflake riming

Supporting Information:

- Text S1 and Figures S1–S4
- Table S1

Correspondence to:

J. Leinonen,
jussi.s.leinonen@jpl.nasa.gov

Citation:

Leinonen, J., and W. Szyrmer (2015), Radar signatures of snowflake riming: A modeling study, *Earth and Space Science*, 2, 346–358, doi:10.1002/2015EA000102.

Received 10 FEB 2015

Accepted 17 JUL 2015

Accepted article online 29 JUN 2015

Published online 25 AUG 2015

©2015. The Authors.

This is an open access article under the terms of the Creative Commons Attribution-NonCommercial-NoDerivs License, which permits use and distribution in any medium, provided the original work is properly cited, the use is non-commercial and no modifications or adaptations are made.

Radar signatures of snowflake riming: A modeling study

Jussi Leinonen¹ and Wanda Szyrmer²
¹Jet Propulsion Laboratory, California Institute of Technology, Pasadena, California, USA, ²Department of Atmospheric and Oceanic Sciences, McGill University, Montreal, Quebec, Canada

Abstract The capability to detect the state of snowflake riming reliably from remote measurements would greatly expand the understanding of its global role in cloud-precipitation processes. To investigate the ability of multifrequency radars to detect riming, a three-dimensional model of snowflake growth was used to generate simulated aggregate and crystal snowflakes with various degrees of riming. Three different growth scenarios, representing different temporal relationships between aggregation and riming, were formulated. The discrete dipole approximation was then used to compute the radar backscattering properties of the snowflakes at frequencies of 9.7, 13.6, 35.6, and 94 GHz. In two of the three growth scenarios, the rimed snowflakes exhibit large differences between the backscattering cross sections of the detailed three-dimensional models and the equivalent homogeneous spheroidal models, similarly to earlier results for unrimed snowflakes. When three frequencies are used simultaneously, riming appears to be detectable in a robust manner across all three scenarios. In spite of the differences in backscattering cross sections, the triple-frequency signatures of heavily rimed particles resemble those of the homogeneous spheroids, thus explaining earlier observational results that were compatible with such spheroids.

1. Introduction

Precipitation is one of the key uncertainties in the present understanding of the Earth's atmosphere-ocean system. Particularly in numerical weather prediction and climate models, the representation of precipitation is currently one of the weakest links [Stephens *et al.*, 2010], due in part to the deficiencies in the modeling of the underlying microphysical processes that govern the formation and growth of precipitation particles [e.g., Golaz *et al.*, 2013; Suzuki *et al.*, 2013].

The microphysics of atmospheric ice and snow is less well understood than that of liquid hydrometeors, largely because of the complexity and great variability of the particle physical properties, governed by the wider variety of growth processes. Atmospheric ice crystals and snowflakes can grow via vapor deposition, by sticking together to form larger snowflakes (i.e., aggregation) and by riming, wherein snowflakes collect supercooled water droplets, which freeze on contact with ice. Besides snowflake growth, the riming of snow is of importance for secondary ice particle formation [Hallett and Mossop, 1974] and for wet removal of aerosols from the atmosphere [Poulida *et al.*, 1998] and has an impact on the spatial distribution, extent and lifetimes of clouds and on precipitation efficiencies [Saleeby *et al.*, 2011]. Moreover, the observed variability of the atmospheric melting layer (depth, peak-to-rain reflectivity, snow-to-rain velocity, backscatter differential phase, and radar signal attenuation) can be related to the degree of riming in the precipitating snow [Zawadzki *et al.*, 2005; Trömel *et al.*, 2014; von Lerber *et al.*, 2015]. Icy precipitation is common in the high latitudes, but snowflakes also often form closer to the equator at high altitudes and later melt as they reach the higher temperatures closer to the surface.

One reason for the gap in the understanding of ice and snow processes is the lack of observational support for the ice microphysics models. The proposed representations of riming rely on assumptions derived mainly from laboratory studies [Lew *et al.*, 1986a, 1986b] and numerical simulations [Wang and Ji, 2000]. In situ microphysical observations can be very challenging due to instrumental difficulties in the measurement of characteristics of individual ice and snow particles, including rimed mass. Furthermore, observations in the higher atmospheric layers require research aircraft and specialized equipment. Only a limited number of microphysical observations include investigations of the contribution of riming within different events [e.g., Reinking, 1975; Mosimann *et al.*, 1994; Barthazy and Schefold, 2006; Stark *et al.*, 2013].

Remote measurements are the only feasible way to implement truly global snowfall observations, but most remote sensing techniques cannot distinguish between the different growth processes, as the relationship between radar observables and microphysical quantities is nonunique. The uncertainties in linking the radar reflectivity with microphysics are related to the scattering calculations and the unknown details of particle structure. A better understanding of the structure of the growing snow particles is required in order to create a realistic particle model with varying densities and irregular morphologies [e.g., Petty and Huang, 2010; Tyynelä *et al.*, 2011; Tyynelä and Chandrasekar, 2014].

Three-frequency radar has been suggested as a technology that can reveal information about the shape of snowflakes, thus potentially identifying the processes that were responsible for their growth [Kneifel *et al.*, 2011]. In this method, the joint behavior of two dual-wavelength ratios (DWR), or ratios of radar reflectivities at different wavelengths, is examined. The use of the ratio of two reflectivities eliminates the effect of the number concentration and provides information about the snowflake size; adding a third frequency adds further information about the shape and structure. Together with the capability of radar to penetrate cloud and precipitation structures, and the ability to operate radars on board satellites, this method could enable global observations of these processes.

Experimental evidence for the feasibility of the triple-frequency technique has been provided by Leinonen *et al.* [2012] and Kulie *et al.* [2014]. A key feature of these studies was to compare the behavior of detailed aggregate snowflake models to that of homogeneous spherical and spheroidal models. Their results demonstrated that the aggregate and spheroid models occupy different regions of the triple-frequency space. However, their results also revealed many cases where the spheroidal snowflakes fit the observed triple-frequency signatures better than the modeled aggregates. More recently, a modeling study by Leinonen and Moisseev [2015] showed that unrimed aggregate snowflake models cannot reproduce the spheroid-like signatures. While the authors of those studies have speculated that riming might cause such signatures, with Stein *et al.* [2015] suggesting a reason as to why this may be the case, no concrete evidence to support this has so far been available.

In this study, we provide the first modeling results of radar scattering from rimed snowflakes generated with a combined riming-aggregation algorithm. This algorithm generates volumetric three-dimensional models of snowflakes, whose scattering properties are computed using the discrete dipole approximation (DDA) method. The results show that the riming clearly shifts the triple-frequency signatures of the snowflakes, suggesting that triple-frequency radar can be used to detect riming, and providing an explanation of the spheroid-like signatures observed before.

2. Methodology

2.1. Aggregation

In the midlatitudes, an important part of the total snowfall is in the form of aggregates [Hosler *et al.*, 1957; Hobbs *et al.*, 1974]. Fujiyoshi and Wakahama [1985], based on the observation results of snow aggregates, concluded that for precipitation rates below 4 mm h^{-1} , riming is more important than deposition in increasing precipitation intensity, except for cloud layers at temperatures around -15°C . Harimaya and Sato [1989] found that the contribution of riming to the total snowfall was higher than 50% during the examined snowfall event. Field experiments by Mitchell *et al.* [1990], Borys *et al.* [2003], and McCormick [2009], mainly in winter orographic precipitation, determined that the amount of accreted supercooled water can account for 20–50% of the total snow mass. In general, growth by deposition is expected to have a relatively small contribution to snowflake growth in the conditions of moderate-to-heavy riming. In contrast, the aggregation process can play an important role in the precipitation growth via riming.

Using the aggregation model that was described in detail by Leinonen [2013], we generated volumetric three-dimensional models of rimed aggregates of ice crystals. In this study, we concentrate on the effect of riming on the scattering properties; furthermore, Leinonen and Moisseev [2015] found that the crystal type has little effect on the triple-frequency signatures. Accordingly, we only used one combination of crystal shape and size in this article: dendrites generated using the algorithm by Reiter [2005], with empirical size-thickness relations of Pruppacher and Klett [1997], and maximum diameters d sampled from the exponential distribution

$$p(d) = \lambda_{\text{cry}} \exp(-\lambda_{\text{cry}} d). \quad (1)$$

where the slope parameter is fixed at $\lambda_{\text{cry}}^{-1} = 0.65 \text{ mm}$. We selected dendrites because of their common occurrence in the atmosphere and their ability to aggregate efficiently. McCormick [2009] discusses the factors that can contribute to a large fraction of the observed snowfall being composed of dendritic crystals, even if the dendrites are expected to grow in a rather narrow temperature interval and only at water saturation conditions. The riming efficiency of dendrites is also expected to be relatively high “since they have more intricate small branches that enable them to capture droplets with higher efficiency” [Wang, 2002]. The minimum and maximum size of the crystals were set at 0.1 and 3.0 mm, respectively, roughly reflecting the natural range of variability [Pruppacher and Klett, 1997]. The assumption of fully dendritic crystals here is somewhat simplified: dendritic growth occurs only when the ventilation velocity exceeds a certain threshold [e.g., Keller and Hallett, 1982], starting around a diameter of 0.15 mm and exhibiting significant dendritic features from about 0.4 mm up [Korolev et al., 2000]. However, at small sizes, the limited resolution of our volumetric models causes the crystals to lose detail, becoming more resemblant of sector plates in appearance.

The aggregation model takes a user-specified number N of ice crystals as input and produces an aggregate by assembling them together using approximations of the physics of aggregate formation. To simulate the partial horizontal alignment of snowflakes in the atmosphere, the shortest principal axis of each aggregate is aligned at a normally distributed random angle, with a mean of 0° and a standard deviation of 40° , following [Huang et al., 2010]. The aggregates are composed of cubic volume elements with a side of $40 \mu\text{m}$ each.

2.2. Riming Process

The major addition to the aggregation algorithm was the ability to simulate the riming of the aggregates. The riming is reproduced by adding single ice volume elements to the bottom of the snowflake, one at a time. The droplets are added on the snowflake from below, effectively assuming that the droplet terminal velocity is negligible compared to that of the much larger snowflake. The position of the droplets on the horizontal plane is sampled from a uniform distribution over the horizontal cross section of the snowflake, thus neglecting aerodynamic effects that may cause rime to gather preferentially on different parts of the snowflake. We expect the error introduced by this approximation to be small, especially for heavier riming, because the snowflake is rotated due to aerodynamically induced tumbling as well as reoriented by the shifting of the mass distribution due to riming, causing the droplet distribution on the surface to even out over time. To simulate roughly the noninstantaneous freezing of supercooled water as it contacts the ice, the droplets are allowed to penetrate a predefined distance into the structure, if vacant space is available. We set the maximum penetration depth at $120 \mu\text{m}$.

The small size of riming droplets limits the resolution of the model. The mode of frozen droplets on natural ice particles was at about $30 \mu\text{m}$ in the observations by Nakaya [1954]. The results presented by Mosimann et al. [1994] show two modes for planar (including dendrites) and columnar snow crystals, peaking at diameters of 20 and $60 \mu\text{m}$, respectively. The mean droplet diameter collected by snowflakes rimed in mixed orographic clouds ranges between 10 and $18 \mu\text{m}$ [Lowenthal et al., 2011]. As the size of the volume elements in our model is $40 \mu\text{m}$, somewhat larger than most of the diameters given above, the shape of the droplets cannot be modeled at finer than single-element resolution.

Published studies propose different ways to quantify the accumulation of rime. Mosimann et al. [1994] proposed a scale of six degrees of riming based primarily on a visual rating of the rime coverage of the ice surface area. A quantitative parameter that is commonly used in literature is the rimed mass fraction. In our algorithm, the total amount of riming that a snowflake collects is controlled by the parameter that we term the effective liquid water path (ELWP). This is defined as $I_e = I E_{\text{rim}}$; the physical liquid water path (LWP) I that the snowflake falls through, multiplied by the riming efficiency E_{rim} . In other words, the ELWP describes what the liquid water path would be, if riming 100% efficient. In reality, the efficiency for a given droplet size is dependent in a complex way upon the size, shape, density, and fall velocity of the snowflake, which change as riming proceeds [Lew et al., 1986a, 1986b; Wang and Ji, 2000]. The same ELWP may represent different LWPs for individual snowflakes, depending on their size, shape, and rimed fraction. The size of cloud droplets may also modify significantly the LWP represented by a given ELWP, as well. However, by fixing the ELWP, we ensure that the snowflakes receive roughly the correct rimed mass, even if our “droplets” are somewhat larger than they would realistically be. The variation of E_{rim} in theory and experiments is summarized in the supporting information Text S1 and Figure S1.

Considering that the size and velocity of the droplets are negligible in comparison to those of snowflakes, the mass m of a rimed snowflake grows at a rate

$$\frac{dm}{dl_e} = A \quad (2)$$

where A is the cross-sectional area of the snowflake, which is computed directly by projecting the snowflake on the horizontal plane. Generally, as mass increases, so does the area, which further increases the capability of the rimed snowflake to collect droplets. We account for this positive feedback by recalculating A repeatedly during the riming process. We also adjust the orientation of the particle as the distribution of mass within the snowflake changes, rotating it to the partial alignment described in section 2.1. The rimed aggregate generation algorithm is summarized in a flowchart in the supporting information Figure S2.

2.3. Riming Scenarios

In nature, riming occurs together with crystal growth by vapor deposition and with snowflake aggregation. The temporal order and the relative importance of these processes depend on the microphysical conditions of the particular case. In general, graupel can originate from rimed ice crystals, from their aggregates or from frozen drops. In snowstorms observed by *Reinking* [1975], the graupel formed primarily on rimed ice crystals, mostly planar and radiating crystals. Investigations of *Scott and Hobbs* [1977] point out that the primary sources of graupel embryos are rimed ice crystals in continental clouds, and frozen large drops after collisions with ice particles in maritime clouds. The formation of heavily rimed graupel-like snow via riming growth of snow aggregates has also been shown to be important for reproducing the microphysical structures of lake-effect storms [*Iguchi et al.*, 2012]. We formulated three reference processes to represent different, somewhat idealized, growth scenarios for snowflakes.

First, we considered conditions where aggregation and riming are undergoing simultaneously in a population of ice crystals. In this scenario (denoted as riming model A), the ELWP that is collected by the snowflake is applied evenly during the aggregation process. For an initial ensemble of N ice crystals, there are a total of $N-1$ collision-aggregation events. Riming equal to an ELWP of $l_e/(N-1)$ is applied to each ice crystal, or cluster of crystals, separately after each such event. Hence, partially rimed snowflakes can still aggregate in this model.

In the second scenario (model B), we allowed the entire aggregation process to take place without any riming and subsequently applied the entire ELWP on the resulting aggregate. Such a scenario could occur when aggregation at higher altitudes depletes the number concentration of snowflakes and decreases their fall velocity dispersion [*Mitchell et al.*, 2006] sufficiently such that no significant aggregation is taking place any longer once the snowflakes fall into a supercooled water layer. This process resulted in a smoother outer surface of the snowflake than the simultaneous riming process.

In the third scenario (model C), we instead sought to reproduce conditions where, in a layer of supercooled water, droplets freeze (perhaps as they contact an ice nucleus). After this, they begin to grow rapidly by collecting rime. In contrast to scenarios A and B, we only created single ice crystals or very small (number of crystals $1 \leq N \leq 5$) aggregates, and produced different degrees of riming, and consequently differently-sized rimed aggregates, by varying the ELWP. For the largest particles produced with model C, ELWP was roughly 6.0 kg m^{-2} .

In models A and B, the ELWP is fixed, and therefore, the number of ice crystals in each snowflake controls their mass and size. On the other hand, in model C, the snowflake size is mainly determined by the amount of rime it collects before falling out of the supercooled water layer.

Figure 1 illustrates the change in snowflake shape with increased riming for model B. It is apparent that the most heavily rimed particles at $l_e = 2.0 \text{ kg m}^{-2}$ have lost the features of the aggregates and become mostly shapeless. This demonstrates that the range of riming explored here covers the transition from unrimed aggregates to heavily rimed, graupel-like snowflakes.

2.4. Snowflake Samples

In scenarios A and B, the varying number of crystals per aggregate controls the mass and size of the snowflakes. These scenarios were explored at different degrees of riming, with ELWPs of 0.0, 0.1, 0.2, 0.5, 1.0, and 2.0 kg m^{-2} . The choice of this range of values was motivated by values of LWP published in the literature: The average LWP derived by *Wang et al.* [2013] from satellite microwave radiometer and CloudSat radar data during 4 years for all snowing clouds was 0.074 kg m^{-2} . The highest mean LWP was retrieved for horizontally

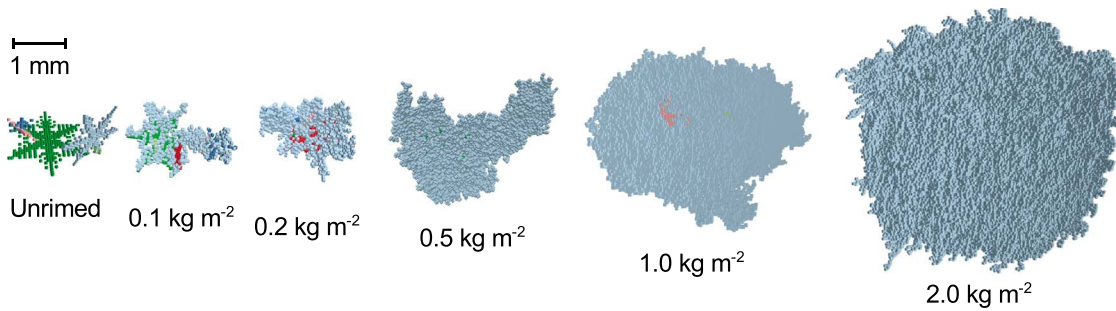


Figure 1. The growth and deformation of the model snowflakes with riming at different values of the effective liquid water path. These snowflakes were generated using the process described for riming model B in section 2.3. Each cubic volume element is 40 μm wide, and all the snowflakes are on the same scale, as shown in the top left corner. The original, unrimed ice crystals are colored in each image in order to distinguish them from the ice formed by riming.

extended shallow clouds and the lowest values for isolated shallow clouds. However, in general, the derived LWP distribution is broad, having a very large spread with the maximum reaching 1 kg m^{-2} for extended shallow and deep systems. The LWP values calculated in winter precipitation during the Light Precipitation Experiment (LPVEx) range from 0.030 to 0.625 kg m^{-2} [Lautaportti *et al.*, 2012]. During the Towards an Optimal estimation based Snow Characterization Algorithm (TOSCA) project, devoted to snowfall observations, the derived LWP reached 0.8 kg m^{-2} [Löhnert *et al.*, 2011]. For deep convective clouds, Sheu *et al.* [1997] report values of over 2.0 kg m^{-2} , and Rosenfeld and Woodley [2000] observed a liquid water content of 1.8 g m^{-3} in temperatures above -38°C , which translates to a LWP of 1.8 kg m^{-2} for a column height of 1 km (and much higher for typical cumulonimbus cloud heights).

In scenario C, the snowflake growth is driven primarily by the riming process, so only one data set was derived from this scenario.

We used the procedure described earlier by Leinonen and Moisseev [2015] to draw a sample from each data set: the interval between zero and the maximum diameter D_{max} was divided into 55 size bins, and rimed aggregates were generated until each bin contained at least 10 of them. Hence, a sample of the rimed aggregates was obtained, roughly uniform in size. D_{max} was set to 22 mm for scenarios A and B and to 8 mm for scenario C. The minimum size, D_{min} , depends on the scenario: the lower limit is set by the minimum dendrite crystal size of 0.1 mm, but in scenarios A and B where the amount of riming was fixed for each data set, the riming process causes even the smallest snowflakes to grow considerably, and thus D_{min} becomes larger, up to 2.8 mm at $I_e = 2.0 \text{ kg m}^{-2}$ for both scenarios A and B. The diameter D was defined as the diameter of the minimum enclosing sphere of the rimed snowflake.

2.5. Scattering Properties

We computed the scattering properties of the snowflakes using the discrete dipole approximation (DDA), implemented in the ADDA software [Yurkin and Hoekstra, 2011]. We computed the scattering properties at four frequencies: 9.7 GHz (X band), 13.6 GHz (Ku band), 35.6 GHz (Ka band), and 94.0 GHz (W band). For the sake of brevity, and to concentrate on triple-wavelength analysis, the results of the X band computations are only shown in the supporting information. Orientation averaging was not performed individually for each particle, but since each snowflake is rotated to partial horizontal alignment as described in section 2.1, the snowflake ensemble as a whole can be considered orientation averaged. The complex refractive indices of ice at each frequency were interpolated from the tables of Warren and Brandt [2008].

The scattering computations for equivalent spheroidal snowflakes were performed with the T-matrix method, using the toolkit of Leinonen [2014] based on the code of Mishchenko and Travis [1998]. The properties of the spheroids were determined as follows: First, we fitted relations for the axis ratio f and mass m of the aggregate models using the forms

$$f = ar_g + b \quad (3)$$

$$m = \alpha' r_g^{\beta'} \quad (4)$$

where a , b , α' , and β' are fitted coefficients and r_g is the radius of gyration, defined as

$$r_g = \sqrt{\frac{1}{V} \int_V (\mathbf{r} - \mathbf{r}_{\text{CM}})^2 d\mathbf{r}} \quad (5)$$

where the integral is taken over the particle volume V and \mathbf{r}_{CM} is the center of mass. Then for each spheroid diameter, we computed the axis ratio and the mass from (3) and (4), respectively. Thus, the equivalent spheroid is defined as a spheroid with mass and radius of gyration equal to its corresponding aggregate. We found that matching the radii of gyration gave a better correspondence between backscattering properties of the spheroid and the detailed snowflake than either using a solid ice spheroid or a soft spheroid with a matched maximum diameter. The model of *Leinonen et al.* [2013] suggests a reason for this: the average distribution of mass within a snowflake is shown to follow the Gaussian distribution, whose width is determined by the standard deviation, which is equivalent to the radius of gyration computed one-dimensionally. In practice, the radius of gyration can be difficult to measure, but the calculations from our model indicate that it can be estimated empirically from the maximum diameter as

$$r_g = 0.287 D. \quad (6)$$

with a root-mean-square relative error of 4.7%. With the mass, size, and axis ratio, and hence the density, determined, the corresponding effective refractive index was computed using the Maxwell-Garnett effective medium approximation.

2.6. Triple-Wavelength Analysis

The dual-wavelength ratio is defined as the ratio of the equivalent radar reflectivities at two different frequencies. To obtain these, we computed the equivalent reflectivity for the K_u , K_a , and W bands; this is defined as

$$Z_e = \frac{\lambda^4}{\pi^5 |K_w|^2} \int_0^{D_{\max}} \sigma(D) N(D) dD \quad (7)$$

where λ is the wavelength, $\sigma(D)$ is the backscattering cross section, and $N(D)$ is the particle size distribution. The dielectric factor K_w is defined as $K_w = (n_w^2 - 1)/(n_w^2 + 2)$, where n_w is the complex refractive index of water at the given frequency, determined in this work at 10°C temperature.

Individual aggregates of similar size and mass can give different results for the backscattering cross section, which makes it somewhat complicated to compute the integral in (7), but it can be approximated using the sample average of the integrand, as discussed by *Leinonen and Moisseev* [2015]. For small diameters, backscattering cross sections are not available from the DDA models, as explained in section 2.4. For the purposes of computing the dual-frequency ratios, the interval $[0, D_{\min}]$ was filled in using the T matrix backscattering cross section σ_{TM} (see section 3.2) for the same snowflake data set. Therefore, we used the approximation

$$\begin{aligned} & \int_0^{D_{\max}} \sigma(D) N(D) dD \\ & \approx \int_0^{D_{\min}} \sigma_{\text{TM}}(D) N(D) dD + (D_{\max} - D_{\min}) \langle \sigma(D) N(D) \rangle_{D_{\min} \leq D \leq D_{\max}} \\ & \approx \int_0^{D_{\min}} \sigma_{\text{TM}}(D) N(D) dD + \frac{D_{\max} - D_{\min}}{N_{\text{agg}}} \sum_{i=1}^{N_{\text{agg}}} \sigma_i N(D_i) \end{aligned} \quad (8)$$

where the sum is taken over the N_{agg} simulated snowflakes in the data set.

For the snowflake particle size distribution $N(D)$, we used the exponential distribution

$$N(D) = N_0 \exp(-\Lambda_s D) \quad (9)$$

where N_0 is the intercept parameter and Λ_s is the inverse scale parameter. The triple-wavelength curves shown in this paper are derived by varying Λ_s , whose inverse Λ_s^{-1} controls the size of snowflakes in the distribution. Accordingly, the average size of snowflakes increases parallel to the triple-wavelength curves. N_0 is a constant scaling factor and as such is eliminated when computing dual-frequency ratios.

3. Results

3.1. Microphysical Properties

In naturally occurring snowflake growth by riming, the accreted droplets are attached to the bottom of the snowflake that is aerodynamically aligned to have its maximal dimension oriented roughly horizontally. This leads to an increase in its roundness, mass and density, but in the early stages of riming, this is not

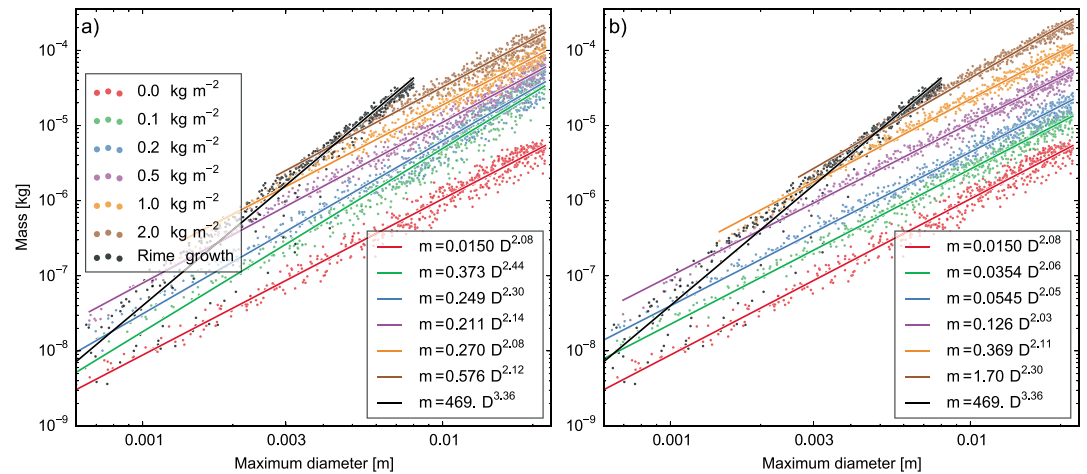


Figure 2. The mass-dimensional relationships of the rimed snowflakes studied in this paper. The different colors correspond to different ELWPs as shown in the legends. (a) For the snowflakes created with riming model A (simultaneous aggregation and riming). The fitted power-laws are given in SI units on the bottom right. (b) As in Figure 2a but for the snowflakes generated from model B (aggregation followed by riming). The results for model C are also shown in both figures, colored black.

accompanied by a significant increase in the particle maximum size. Consequently, particle density remains a decreasing function of size: the prefactor α in the mass-size power law

$$m = \alpha D^\beta \quad (10)$$

increases, but the exponent β retains a value close to 2; Westbrook *et al.* [2004] present theoretical reasons for an exponent of exactly 2 for aggregation-driven growth. Examples of field measurements that confirm the lack of increase in β for lightly and moderately rimed particles are given by Morrison and Milbrandt [2015]. The original shape of the particle is lost only when the rimed fraction becomes significant, and the aggregates of rimed crystals and heavily rimed aggregates become graupel-like snow. For this type of particles, the mass-size relationships reported by Locatelli and Hobbs [1974] still show a decrease of density with increasing size, since their $\beta < 2.5$. A mass-size exponent close to 3 describes lump and hexagonal graupel particles.

We determined mass-size power laws of the form (10), where α and β were obtained by regression analysis, for the different types of rimed aggregates. These relationships are illustrated in Figure 2. Notably, riming models A and B are seen to produce scaling exponents β between 2.0 and 2.5 (though usually closer to 2.0), while model C results in $\beta = 3.36$. This is due to the different dominant growth processes: The growth is driven by the aggregation process in models A and B and by riming in model C.

An empirical value of $\beta > 3$ is possible in scenario C because the riming also increases the roundness of the snowflake. Clearly, such growth could not continue indefinitely, as the density would eventually exceed that of solid ice, but Figure 2 shows that this exponent gives a good fit over the range of diameters studied here. Some models of graupel suggest that the particle density may increase with size because droplets can penetrate deeper into larger, faster-falling particles, and such an assumption was incorporated into the parametrization of Geresdi [1998]; however, this is not reproduced in our model as the penetration depth is held constant. In any case, the m - D relation obtained for our model C, $m = 469D^{3.36}$, agrees well with the experimental power law of Heymsfield and Wright [2014, their equation (3)], which gives $m = 431D^{3.33}$ when converted to SI units.

The difference between models A (simultaneous aggregation and riming) and B (where riming takes place after aggregation) is demonstrated by the differences in how the rimed fraction (the ratio of rimed ice mass to total ice mass) behaves with snowflake size, as shown in Figure 3. The rimed fraction is not constant in either case. In model A, the rimed fraction first decreases with increasing size, as aggregation dominates growth, then tends toward values close to 1. The minimum is found around $D = 3$ mm. On the other hand, with model B, the rimed fraction decreases monotonically with size. Overall, model A produces significantly larger rimed fractions than model B.

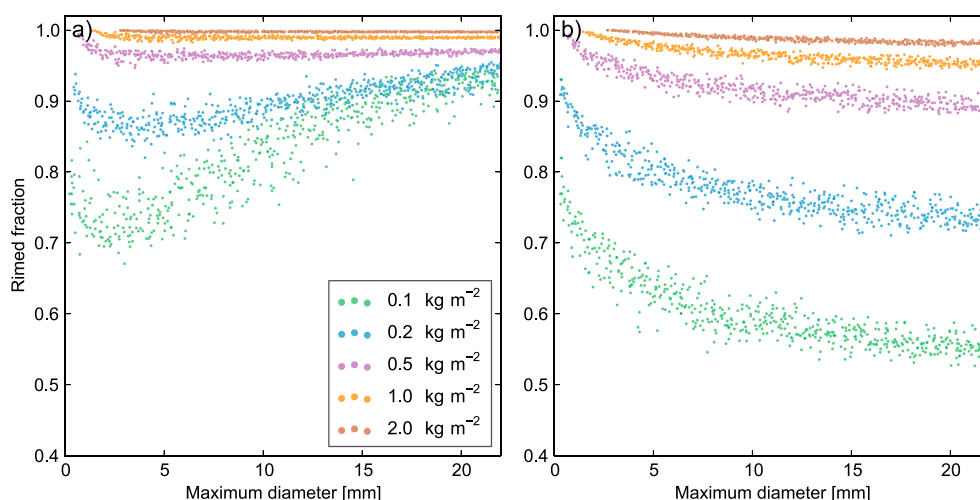


Figure 3. The behavior of the rimed fraction of snowflakes with size. The different ELWPs are color coded, as in Figure 2. (a) For riming model A. (b) For model B.

3.2. Backscattering Properties

We computed the backscattering cross sections of the snowflakes and compared them with their equivalent spheroidal models. These are shown in Figure 4; the results for the X band can be found in the supporting information Figure S3.

The homogeneity of the scatterer in the spheroid approximation causes the backscattering cross section to saturate at much smaller sizes. In detailed snowflake models, structural features exist at scales much smaller than the particle size, therefore avoiding such saturation. The effects of small inhomogeneities on the behavior of the backscattering from snowflakes were discussed in the unrimed case by *Leinonen et al.* [2013]. Previous studies [e.g., *Leinonen et al.*, 2012] had speculated that the backscattering properties of rimed snowflakes would resemble those of spheroids because the structure of rimed snow is more homogeneous. The results presented here for models A and B seem to contradict those expectations: The correspondence between aggregates and spheroids seems to break down at least as rapidly for rimed snowflakes as it does for the unrimed ones. As seen before for unrimed snow by, e.g., *Tyynelä et al.* [2011], the difference between the detailed rimed aggregate and the equivalent spheroid can be up to 2 orders of magnitude for snowflake sizes larger than the wavelength λ . In general, the breakdown between the two models occurs at $D \approx \lambda/2$ for unrimed snow. For rimed snow, this happens somewhat earlier, which is probably because of the higher density in dense rimed particles resulting in a higher effective refractive index.

With model C, on the other hand, the backscattering cross section of the graupel-like particles generated by it agree with the results for the spheroids relatively well throughout the size range up to 8 mm, even at the W band. Interestingly, the DDA model results from these particles show signs of resonances, which occur around $D = 7.4$ mm at the Ka band and at $D = 2.9$ mm at the W band. The magnitude of these resonance effects appears to be similar to those exhibited by the spheroid models, although their locations are not aligned.

3.3. Triple-Frequency Signatures

The triple-wavelength plots for the snowflakes are shown in Figure 5. The curves are derived by computing the reflectivity for each band using (7), (8), and (9), varying the characteristic size Λ_s^{-1} between 0 and 11 mm (models A and B) or 0 and 4 mm (model C), and then plotting the relation of two dual-wavelength ratios as a function of Λ_s . An alternative plot, using the X band instead of the Ku band, can be found in the supporting information Figure S4.

Despite the different microphysics, the overall behavior of the DWR curves with increasing ELWP is the same for both riming models A and B: $DWR_{Ka/W}$ peaks at approximately 8 dB for unrimed and lightly rimed snowflakes, and the riming does not have much effect on the curves until the ELWP reaches 0.5 kg m^{-2} . LWPs of this magnitude have been reported in field experiments by, for example, *Wang et al.* [2013] for a shallow precipitating cloud and by *Kneifel et al.* [2010] for the TOSCA campaign. For higher ELWP, the peak $DWR_{Ka/W}$ increases further to 14 dB (model A) or 13 dB (model B). Heavier riming also causes the $DWR_{Ku/Ka}$ to increase

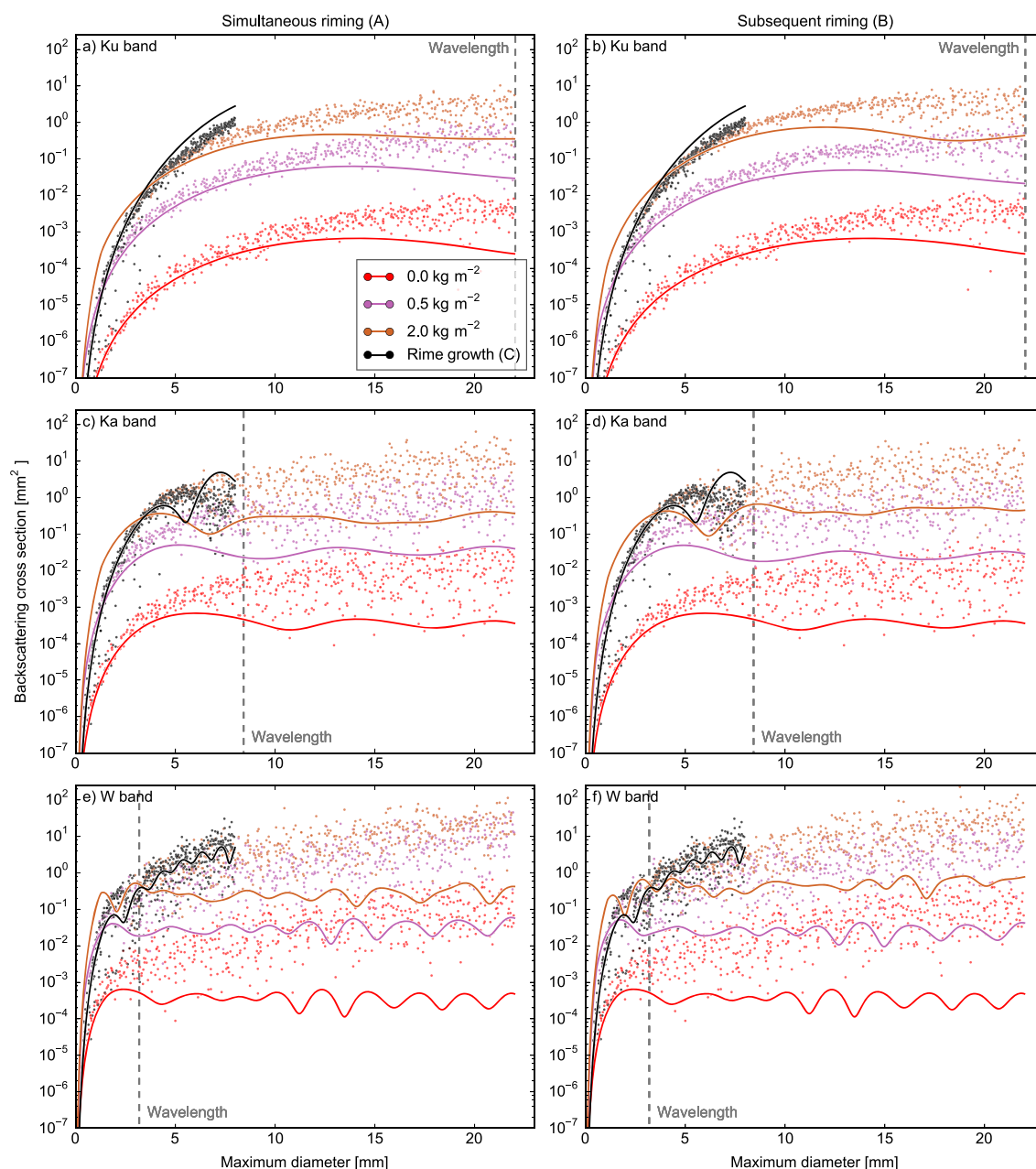


Figure 4. The backscattering cross section of snowflakes by size. The dots give the cross sections for the individual aggregates, while the solid lines show the backscattering cross sections for the equivalent spheroids, determined as described in section 3.2. Only the cases with effective liquid water paths of 0.0, 0.5, and 2.0 kg m⁻² are shown. (a) For riming model A, at K_u band. (b) As in Figure 4a but for riming model B. (c and d) As in Figures 4a and 4b but for K_a band. (e and f) As in Figures 4a and 4b but for W band. In each figure, the result from riming model C is shown in black for comparison.

less rapidly with increasing $DWR_{K_a/W}$. Model C produces a peak $DWR_{K_a/W}$ of approximately 12 dB. The curve from this model is very similar to those given by models A and B at an ELWP of 1.0 kg m⁻².

Unlike the unrimed aggregates, the triple-frequency signatures of the heavily rimed snowflakes, as well as the variable-riming snowflakes of model C, reside mostly in the region of the triple-wavelength plots that earlier studies have found to contain the spheroidal snowflakes. This is true even for the heavily rimed aggregates from models A and B, whose backscattering cross sections do not agree with those of their spheroidal approximations.

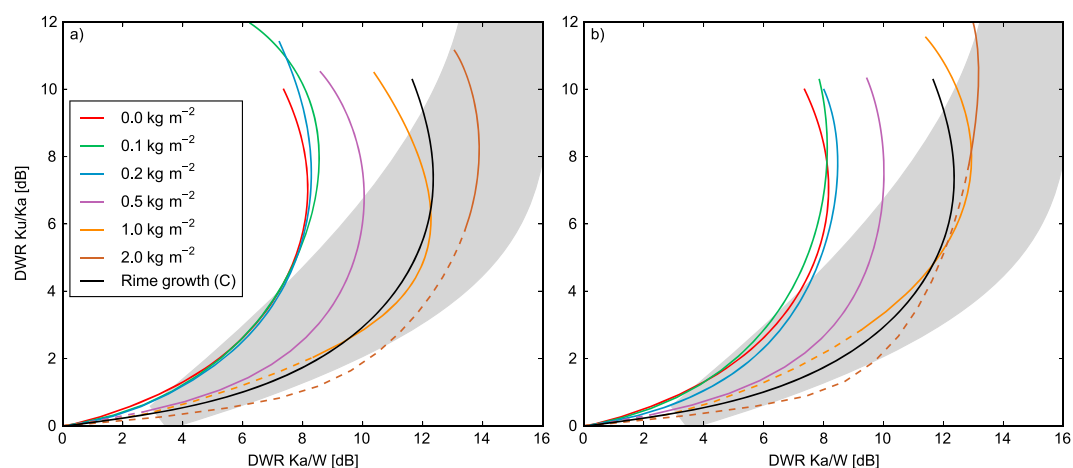


Figure 5. Triple-wavelength plots for the rimed aggregates. The dual-wavelength ratios are computed for exponential size distributions; the characteristic size Λ_s^{-1} increases parallel to the curves. The dashed lines show areas where the spheroids that are used to model small particles contribute more than 25% of the total reflectivity. The shaded area encloses the region occupied by homogeneous spheroidal snowflake models. (a) For riming model A. (b) For model B.

4. Discussion and Conclusions

This article documents the first results of radar backscattering by rimed snowflakes modeled with a snowflake generation algorithm that includes both aggregation and riming. We present results for three different idealized riming scenarios: aggregation growth simultaneous with riming (A), aggregation growth followed by riming (B), and riming-driven growth (C). While models A and B are microphysically different, they exhibit remarkably similar radar scattering properties, both in the absolute values of the backscattering cross section and in their triple-frequency signatures. Meanwhile, model C produces backscattering cross sections that are larger than those of the particles of the same size from models A and B; despite this, its triple-frequency signature is very similar to heavily rimed aggregates from models A and B.

The results highlight the importance of the underlying snow growth process to the backscattering properties of snowflakes. The backscattering cross sections of the rimed snowflakes can be orders of magnitude higher than those of unrimed ones of the same size. Furthermore, even the details of the riming process can cause differences between bulk microphysical properties such as the mass-diameter relationship and consequently also the backscattering properties: models A and B generate snowflake ensembles with mass-diameter exponents of roughly 2, while model C gives rise to an exponent larger than 3. Consistently with this, the backscattering cross section of snowflakes from model C increases more rapidly with size than those from models A and B.

Riming seems to have a robust signal in the triple-frequency signatures, shifting them to larger $DWR_{Ka/W}$ for large rimed aggregates and to smaller $DWR_{Ku/Ka}$ for smaller ones. Despite the microphysical differences, the joint behavior of $DWR_{Ka/W}$ and $DWR_{Ku/Ka}$ is consistent across all riming models studied. For heavily rimed particles, $DWR_{Ka/W}$ peaks around 12–14 dB for sufficiently large snowflakes, in agreement with the observations of *Leinonen et al.* [2012] and *Kulie et al.* [2014]. Additionally, models A and B produce very similar backscattering properties in spite of their different rimed fractions.

While the riming signal is quite robust in ideal conditions, errors that may bias the reflectivity must be properly accounted for in order to correctly identify the presence of riming from radar observations, as the magnitude the signal is fairly modest. The most important potential error source is likely to be attenuation, which is typically weak in dry snow, but can increase significantly in the presence of riming due to the absorption by supercooled liquid water, the amount of which is typically difficult to constrain. In many applications, radar beam collocation between the different frequencies is also an issue. If the radars are able to scan, beam matching can often be achieved in postprocessing by spatially averaging data at the cost of resolution. Furthermore, the studies of *Leinonen et al.* [2012], *Kulie et al.* [2014], and *Stein et al.* [2015] have reported spreads of the order of 1–2 dB in their observations. This can translate to quite significant differences in retrieved ELWP but is still clearly smaller than the dynamic range of the riming signal, up to 6 dB in this study.

Earlier work identified measured triple-frequency signatures that previous modeling studies found incompatible with unrimed aggregates and could only explain them with the uniform spheroid shape approximation. The modeling results obtained in this study strongly suggest that these signatures can be attributed to rimed snow, confirming the earlier conjectures that this was the case. It was also previously suggested that the triple-frequency signatures of rimed snowflakes and spheroids are similar because riming would make snowflake structure more homogeneous, thus causing them to resemble the homogeneous “soft” spheroids. Our results indicate that this view is incomplete. The backscattering cross sections of the rimed snowflakes from model C did agree with those of the spheroids, but the results for heavily rimed aggregates from models A and B diverged from the spheroids by roughly as much as the unrimed aggregates did. Regardless, models A and B produced triple-frequency signatures that were mostly in the spheroid regime.

In earlier work, *Stein et al.* [2015] connected the saturation value of $DWR_{ka/w}$ to the fractal dimension and, consequently, the mass-size exponent β . Our results indicate that even heavy riming need not necessarily be characterized by $\beta \approx 3$, as has been commonly assumed, although in practice this is usually the case. When multiple processes with different fractal characteristics (here, aggregation and riming) contribute to snowflake growth, the description of the structure using a single fractal dimension may be too simplistic. It is encouraging, however, that it appears possible to detect riming with triple-frequency radars, regardless of the originating process.

The identification of triple-frequency radars as instruments that can remotely detect the signal of snowflake riming further adds to their promise for spaceborne observations of global clouds and precipitation. Over the last few years, collocated radars at three frequencies have been operated simultaneously in several experiments, such as that by *Stein et al.* [2015] at Chilbolton, England, and at the Atmospheric Radiation Measurement (ARM) Mobile Facility 2 in Hyttälä, Finland. These field experiments should be expanded in the future to cover different climates and snow types. Together with the modeling efforts, they support the verification of the triple-frequency techniques and contribute to the eventual objective of developing a quantitative three-frequency snowfall retrieval algorithm.

Acknowledgments

The original data used in this study, including the snowflake sizes, masses, and backscattering cross sections, are partially included in the supporting information Table S1; the rest are available from the corresponding author on request (email: jussi.s.leinonen@jpl.nasa.gov). We would like to thank Matthew D. Lebsock (Jet Propulsion Laboratory) and Pavlos Kollias (McGill University) for their support of this study. We also thank two anonymous reviewers for their constructive comments. This research was supported in part by the National Aeronautics and Space Administration (NASA) Aerosol-Clouds-Ecosystem project. The research of J.L. described in this publication was carried out at the Jet Propulsion Laboratory, California Institute of Technology, under contract with NASA.

References

- Barthazy, E., and R. Schefold (2006), Fall velocity of snowflakes of different riming degree and crystal types, *Atmos. Res.*, **82**, 391–398, doi:10.1016/j.atmosres.2005.12.009.
- Borys, R. D., D. H. Lowenthal, S. A. Cohn, and W. O. J. Brown (2003), Mountaintop and radar measurements of anthropogenic aerosol effects on snow growth and snowfall rate, *Geophys. Res. Lett.*, **30**, 1538, doi:10.1029/2002GL016855.
- Fujiyoshi, Y., and G. Wakahama (1985), On snow particles comprising an aggregate, *J. Atmos. Sci.*, **42**, 1667–1674, doi:10.1175/1520-0469(1985)042<1667:OSPCAA>2.0.CO;2.
- Geresdi, I. (1998), Idealized simulation of the Colorado hailstorm case: Comparison of bulk and detailed microphysics, *Atmos. Res.*, **45**(4), 237–252, doi:10.1016/S0169-8095(97)00079-3.
- Golaz, J.-C., L. W. Horowitz, and H. Levy (2013), Cloud tuning in a coupled climate model: Impact on 20th century warming, *Geophys. Res. Lett.*, **40**, 2246–2251, doi:10.1002/grl.50232.
- Hallett, J., and S. C. Mossop (1974), Production of secondary ice particles during the riming process, *Nature*, **249**, 26–28, doi:10.1038/249026a0.
- Harimaya, T., and M. Sato (1989), Measurement of riming amount on snowflakes, *J. Fac. Sci. Hokkaido Univ., Ser.*, **7**(8), 355–366.
- Heymsfield, A., and R. Wright (2014), Graupel and hail terminal velocities: Does a “supercritical” Reynolds number apply?, *J. Atmos. Sci.*, **71**, 3392–3403, doi:10.1175/JAS-D-14-0034.1.
- Hobbs, P. V., S. Chang, and J. D. Locatelli (1974), The dimensions and aggregation of ice crystals in natural clouds, *J. Geophys. Res.*, **79**, 2199–2206, doi:10.1029/JC079i015p02199.
- Hosler, C. L., D. C. Jensen, and L. Goldshlak (1957), On the aggregation of ice crystals to form snow, *J. Meteorol.*, **14**, 415–420, doi:10.1175/1520-0469(1957)014<0415:OTAOIC>2.0.CO;2.
- Huang, G.-J., V. N. Bringi, R. Cifelli, D. Hudak, and W. A. Petersen (2010), A methodology to derive radar reflectivity-liquid equivalent snow rate relations using C-band radar and a 2D video disdrometer, *J. Atmos. Oceanic Technol.*, **27**(4), 637–651, doi:10.1175/2009JTECHA1284.1.
- Iguchi, T., T. Matsui, J. J. Shi, W.-K. Tao, A. P. Khain, A. Hou, R. Cifelli, A. Heymsfield, and A. Tokay (2012), Numerical analysis using WRF-SBM for the cloud microphysical structures in the C3VP field campaign: Impacts of supercooled droplets and resultant riming on snow microphysics, *J. Geophys. Res.*, **117**, D23206, doi:10.1029/2012JD018101.
- Keller, V. W., and J. Hallett (1982), Influence of air velocity on the habit of ice crystal growth from the vapor, *J. Crystal Growth*, **60**(1), 91–106, doi:10.1016/0022-0248(82)90176-2.
- Kneifel, S., U. Löhnert, A. Battaglia, S. Crewell, and D. Siebler (2010), Snow scattering signals in ground-based passive microwave radiometer measurements, *J. Geophys. Res.*, **115**, D16214, doi:10.1029/2010JD013856.
- Kneifel, S., M. S. Kulie, and R. Bennartz (2011), A triple frequency approach to retrieve microphysical snowfall parameters, *J. Geophys. Res.*, **116**, D11203, doi:10.1029/2010JD015430.
- Korolev, A., G. A. Isaac, and J. Hallett (2000), Ice particle habits in stratiform clouds, *Q. J. R. Meteorol. Soc.*, **126**, 2873–2902, doi:10.1002/qj.49712656913.
- Kulie, M. S., M. J. Hiley, R. Bennartz, S. Kneifel, and S. Tanelli (2014), Triple frequency radar reflectivity signatures of snow: Observations and comparisons to theoretical ice particle scattering models, *J. Appl. Meteorol. Climatol.*, **1080**–1098, doi:10.1175/JAMC-D-13-066.1.

- Lautaportti, S., D. Moiseev, P. Saavedra, V. Battaglia, and V. Chandrasekar (2012), C-band dual-polarization radar and microwave radiometer observations of winter precipitation during LPVEx, paper presented at 7th European Conference on Radar Meteorology, Météo-France, 25–29 June.
- Leinonen, J. (2013), Impact of the microstructure of precipitation and hydrometeors on multi-frequency radar observations, PhD thesis, Aalto Univ., Espoo, Finland.
- Leinonen, J. (2014), High-level interface to T-matrix scattering calculations: Architecture, capabilities and limitations, *Opt. Express*, 22(2), 1655–1660, doi:10.1364/OE.22.001655.
- Leinonen, J., and D. Moiseev (2015), What do triple-frequency radar signatures reveal about aggregate snowflakes?, *J. Geophys. Res. Atmos.*, 120, 229–239, doi:10.1002/2014JD022072.
- Leinonen, J., S. Kneifel, D. Moiseev, J. Tyynelä, S. Tanelli, and T. Nousiainen (2012), Evidence of nonspheroidal behavior in millimeter-wavelength radar observations of snowfall, *J. Geophys. Res.*, 117, D18205, doi:10.1029/2012JD017680.
- Leinonen, J., D. Moiseev, and T. Nousiainen (2013), Linking snowflake microstructure to multi-frequency radar observations, *J. Geophys. Res. Atmos.*, 118, 3259–3270, doi:10.1002/jgrd.50163.
- Lew, J. K., D. C. Montague, H. R. Pruppacher, and R. M. Rasmussen (1986a), A wind tunnel investigation on the riming of snowflakes. Part I: Porous disks and large stellars, *J. Atmos. Sci.*, 43, 2392–2409, doi:10.1175/1520-0469(1986)043<2392:AWTIOT>2.0.CO;2.
- Lew, J. K., D. C. Montague, H. R. Pruppacher, and R. M. Rasmussen (1986b), A wind tunnel investigation on the riming of snowflakes. Part II: Natural and synthetic aggregates, *J. Atmos. Sci.*, 43(21), 2410–2417, doi:10.1175/1520-0469(1986)043<2410:AWTIOT>2.0.CO;2.
- Locatelli, J. D., and P. V. Hobbs (1974), Fall speeds and masses of solid precipitation particles, *J. Geophys. Res.*, 79(15), 2185–2197, doi:10.1029/JC079i015p02185.
- Lowenthal, D. H., R. D. Borys, W. Cotton, S. Saleeby, S. A. Cohn, and W. O. J. Brown (2011), The altitude of snow growth by riming and vapor deposition in mixed-phase orographic clouds, *Atmos. Environ.*, 45(2), 519–522, doi:10.1016/j.atmosenv.2010.09.061.
- Löhnert, U., S. Kneifel, A. Battaglia, M. Hagen, L. Hirsch, and S. Crewell (2011), A multisensor approach toward a better understanding of snowfall microphysics: The TOSCA project, *Bull. Am. Meteorol. Soc.*, 92, 613–628, doi:10.1175/2010BAMS2909.1.
- McCormick, H. S. (2009), *Observations and Modeling of Snow Over the Washington Cascades*, Univ. of Washington.
- Mishchenko, M. I., and L. D. Travis (1998), Capabilities and limitations of a current FORTRAN implementation of the T-matrix method for randomly oriented, rotationally symmetric scatterers, *J. Quant. Spectros. Radiat. Transfer*, 60(3), 309–324, doi:10.1016/S0022-4073(98)00008-9.
- Mitchell, D. L., R. Zhang, and R. L. Pitter (1990), Mass-dimensional relationships for ice particles and the influence of riming on snowfall rates, *J. Appl. Meteorol.*, 29(2), 153–163, doi:10.1175/1520-0450(1990)029<0153:MDRFP>2.0.CO;2.
- Mitchell, D. L., A. Huggins, and V. Grubisic (2006), A new snow growth model with application to radar precipitation estimates, *Atmos. Res.*, 82(1–2), 2–18, doi:10.1016/j.atmosres.2005.12.004.
- Morrison, H., and J. A. Milbrandt (2015), The altitude of snow growth by riming and vapor deposition in mixed-phase orographic clouds, *J. Atmos. Sci.*, 72, 287–311, doi:10.1175/JAS-D-14-0065.1.
- Mosimann, L., E. Weingartner, and A. Waldvogel (1994), An analysis of accreted drop sizes and mass on rimed snow crystals, *J. Atmos. Sci.*, 51, 1548–1558, doi:10.1175/1520-0469(1994)051<1548:AAOADS>2.0.CO;2.
- Nakaya, U. (1954), *Snow Crystals: Natural and Artificial*, Harvard Univ. Press, Cambridge, Mass.
- Petty, G. W., and W. Huang (2010), Microwave backscatter and extinction by soft ice spheres and complex snow aggregates, *J. Atmos. Sci.*, 67(3), 769–787, doi:10.1175/2009JAS3146.1.
- Poulida, O., M. Schikowski, U. Baltensperger, J. Staehelin, and H. W. Gaggeler (1998), Scavenging of atmospheric constituents in mixed phase clouds at the high-alpine site Jungfraujoch—Part II. Influence of riming on the scavenging of particulate and gaseous chemical species, *Atmos. Environ.*, 32(23), 3985–4000, doi:10.1016/S1352-2310(98)00131-9.
- Pruppacher, H. R., and J. D. Klett (1997), *Microphysics of Clouds and Precipitation*, 2nd ed., Springer, Dordrecht, Netherlands.
- Reinking, R. F. (1975), Formation of graupel, *J. Appl. Meteorol.*, 14(5), 745–754, doi:10.1175/1520-0450(1975)014<0745:FOG>2.0.CO;2.
- Reiter, C. A. (2005), A local cellular model for snow crystal growth, *Chaos Soliton Fract.*, 23, 1111–1119, doi:10.1016/j.chaos.2004.06.071.
- Rosenfeld, D., and W. L. Woodley (2000), Deep convective clouds with sustained supercooled liquid water down to -37.5°C , *Nature*, 405, 440–442, doi:10.1038/35013030.
- Saleeby, S. M., W. R. Cotton, and J. D. Fuller (2011), The cumulative impact of cloud droplet nucleating aerosols on orographic snowfall in Colorado, *J. Appl. Meteorol. Climatol.*, 50, 604–625, doi:10.1175/2010JAMC2594.1.
- Scott, B. C., and P. V. Hobbs (1977), A theoretical study of the evolution of mixed-phase cumulus clouds, *J. Atmos. Sci.*, 34, 812–826, doi:10.1175/1520-0469(1977)034<0812:ATSOTE>2.0.CO;2.
- Sheu, R.-S., J. A. Curry, and G. Liu (1997), Vertical stratification of tropical cloud properties as determined from satellite, *J. Geophys. Res.*, 102, 4231–4246, doi:10.1029/96JD02867.
- Stark, D., B. A. Colle, and S. E. Yuter (2013), Observed microphysical evolution for two East Coast winter storms and the associated snow bands, *Mon. Weather Rev.*, 141, 2037–2057, doi:10.1175/MWR-D-12-00276.1.
- Stein, T. H. M., C. D. Westbrook, and J. C. Nicol (2015), Fractal geometry of aggregate snowflakes revealed by triple-wavelength radar measurements, *Geophys. Res. Lett.*, 43, 176–183, doi:10.1002/2014GL062170.
- Stephens, G. L., T. L'Ecuyer, R. Forbes, A. Gettleman, J.-C. Golaz, A. Bodas-Salcedo, K. Suzuki, P. Gabriel, and J. Haynes (2010), Dreary state of precipitation in global models, *J. Geophys. Res.*, 115, D24211, doi:10.1029/2010JD014532.
- Suzuki, K., J.-C. Golaz, and G. L. Stephens (2013), Evaluating cloud tuning in a climate model with satellite observations, *Geophys. Res. Lett.*, 40, 4464–4468, doi:10.1002/grl.50874.
- Trömel, S., A. V. Ryzhkov, P. Zhang, and C. Simmer (2014), Investigations of backscatter differential phase in the melting layer, *J. Appl. Meteorol. Climatol.*, 53, 2344–2359, doi:10.1175/JAMC-D-14-0050.1.
- Tyynelä, J., and V. Chandrasekar (2014), Characterizing falling snow using multifrequency dual-polarization measurements, *J. Geophys. Res. Atmos.*, 119, 8268–8283, doi:10.1002/2013JD021369.
- Tyynelä, J., J. Leinonen, D. Moiseev, and T. Nousiainen (2011), Radar backscattering from snowflakes: Comparison of fractal, aggregate and soft-spheroid models, *J. Atmos. Oceanic Technol.*, 28, 1365–1372, doi:10.1175/JTECH-D-11-00004.1.
- von Lerber, A., D. Moiseev, J. Leinonen, J. Koistinen, and M. Hallikainen (2015), Modeling radar attenuation by a low melting layer with optimized model parameters at C-band, *IEEE Trans. Geosci. Remote Sens.*, 53, 724–737, doi:10.1109/TGRS.2014.2327148.
- Wang, P. K. (2002), *Ice Microdynamics*, Academic Press, San Diego, Calif.
- Wang, P. K., and W. Ji (2000), Collision efficiencies of ice crystals at low-intermediate Reynolds numbers colliding with supercooled cloud droplets: A numerical study, *J. Atmos. Sci.*, 57, 1001–1009, doi:10.1175/1520-0469(2000)057<1001:CEOICA>2.0.CO;2.
- Wang, Y., G. Liu, E.-K. Seo, and Y. Fu (2013), Liquid water in snowing clouds: Implications for satellite remote sensing of snowfall, *Atmos. Res.*, 131, 60–72, doi:10.1016/j.atmosres.2012.06.008.

- Warren, S. G., and R. E. Brandt (2008), Optical constants of ice from the ultraviolet to the microwave: A revised compilation, *J. Geophys. Res.*, *113*, D14220, doi:10.1029/2007JD009744.
- Westbrook, C. D., R. C. Ball, P. R. Field, and A. J. Heymsfield (2004), Theory of growth by differential sedimentation, with application to snowflake formation, *Phys. Rev. E*, *70*(2), 21,403, doi:10.1103/PhysRevE.70.021403.
- Yurkin, M. A., and A. G. Hoekstra (2011), The discrete-dipole-approximation code ADDA: Capabilities and known limitations, *J. Quant. Spectrosc. Radiat. Transfer*, *112*, 2234–2247, doi:10.1016/j.jqsrt.2011.01.031.
- Zawadzki, I., W. Szyrmer, C. Bell, and F. Fabry (2005), Modeling of the melting layer. Part III: The density effect, *J. Atmos. Sci.*, *62*, 3705–3723, doi:10.1175/JAS3563.1.